

Model Predictive Control based AGC for Multi-terminal HVDC-connected AC grids

Paul Mc Namara, *Member, IEEE*, Federico Milano, *Fellow, IEEE*

Abstract—Multi-terminal HVDC (MTDC) grids are seen as the enabling technology in the development of massive scale international grids such as the European Supergrid. It is expected that these grids can play a significant role in regulating ac system frequencies. To date, many proportional-integral (PI) controller based techniques have been proposed for frequency regulation in ac MTDC-connected grids. In this paper Model Predictive Control (MPC) is proposed as a means of implementing Automatic Generation Control, while minimising dc grid power losses. The advantages of using MPC versus PI are highlighted with regard to improvements in both frequency and dc grid regulation, while explicitly considering both delays and dc voltage constraints.

Index Terms—Multi-terminal HVDC, Automatic Generation Control, Model Predictive Control.

I. INTRODUCTION

HIGH voltage direct current (HVDC) technology has the potential to radically transform the operation of electrical grids around the world. As large stochastic renewable penetrations provide increasing challenges for the tight regulation of electrical grids, interconnection via HVDC links is seen as a means of aggregating these renewable sources over a wide area. The underlying idea here is that in areas where there is an excess of renewables produced, if this area is connected by an HVDC link to another area capable of absorbing the excess power production, then the excess can be consumed by the connected area, thus allowing both areas to increase their overall renewable penetration [1]. For example, the NordLink HVDC link between Germany and Norway will allow Germany and neighbouring countries to export excess renewable reserves to Norway, where there are large scale hydro reserves. Similarly, Germany and neighbouring countries can import the clean hydro energy back via the HVDC link at times of reduced renewable reserves. This capability is giving rise to the concept of a so-called European “Supergrid”, where a large scale meshed HVDC grid will interconnect grids across Europe [1].

The enabling technology behind the construction of modern HVDC grids is voltage source converter (VSC) technology. VSCs offers significant advantages over traditional line commutated converters (LCCs). VSCs allow independent control of active and reactive powers, and do not consume reactive power. The development of multi-terminal HVDC (MTDC) grids is of particular interest in recent years. In MTDC grids a number of HVDC lines can connect to a single VSC terminal, thus allowing for the creation of meshed dc networks. VSCs in particular enable significant flexibility in these networks in

comparison to LCC based MTDC networks, due to the ability of VSC based MTDC grids to enable bi-directionality of power flows (LCC requires the reversal of the voltage polarity to achieve this, severely limiting the potential for bi-directionality in meshed LCC-based dc grids) [2]. The first MTDC grid in the world was recently built in Zhoushan, China [3].

As the number of VSC connected devices increases in electricity grids it will be desirable for these VSC connections to partake in frequency regulation. The majority of frequency regulation schemes in the literature are based on proportional (P) or proportional-integral (PI) based control approaches. A number of decentralised primary control methods have been proposed in the literature, where the VSC power delivery setpoint loop is augmented by a frequency error term in order to trade off frequency regulation against power setpoint regulation [2], [4], [5]. Several secondary control algorithms based on PI methods have been proposed [4], [6], [7].

Traditionally, P-based primary and PI-based AGC have been temporally decoupled. The primary controllers were designed using proportional control to counteract the initial fast transients associated with the angular frequency deviations at each generator. This use of proportional control in a decentralised fashion generally provides a stable response to a wide range of contingencies, but also results in long term offsets. Thus secondary control uses integral control over longer time scales on the seconds to minutes scale in order to eliminate these long term offsets. When using PI control, however, it is necessary to temporally decouple these two control schemes so that there is no strong interactions between the primary and secondary controls. This has the effect of limiting the gains which can be applied for use with PI-based AGC.

Model predictive control (MPC) is an optimisation based MIMO control technique, which uses state-space predictions in order to form optimal inputs to a system, with respect to a cost function specified by the system designer [8]. Because primary control can be modelled as part of the state-space system representation, when MPC is used for AGC, it is possible for the secondary control to explicitly consider the interactions between primary and secondary control. Thus, MPC based AGC allows for a greater symbiosis between primary and secondary control, in turn allowing for improved overall regulation performance.

MPC has been shown to offer setpoint tracking and robustness performance in a range of power systems applications including secondary frequency control, typically referred to as automatic generation control (AGC) [9]–[11], and voltage control [12], [13]. Additionally, MPC has been suggested for application to the dynamic control of point-to-point HVDC links [14], [15] and for providing predictive optimal power

Paul Mc Namara and F. Milano are with the School of Electrical and Electronic Engineering, University College Dublin, Belfield, Ireland. (e-mails: paul.mcnamara@ucd.ie; federico.milano@ucd.ie).

flow for MTDC systems in [16]. Recently it was shown that MPC could be used as a means of improving AGC performance and robustness for ac areas connected to MTDC grids versus decentralised PI based techniques [11], [17]. In [11], [17], several assumptions were made. First of all, it was assumed that controllers could directly control dc node voltages. Secondly, the controllers assumed that there were no communication delays associated with control (it should be noted that the effect of delays using MPC for point-to-point HVDC links has been considered previously in [18]). Finally, it was assumed that control agents had access to perfect state measurements for use in control.

There are some practical issues associated with the aforementioned assumptions. Typically transmission system operators (TSOs) send a power setpoint to VSCs in HVDC systems, and the internal VSC controllers act to provide the desired power injection into the ac grid controlled by the TSO. Thus, the TSO does not directly control VSC voltages but controls this setpoint, and the VSC will adjust the dc node voltage based on this setpoint. Also, there are typically communication delays associated with AGC in the seconds scale. To date, some of these issues were addressed in [19], [20], where MPC is used to aid AGC by manipulating the VSC setpoints, explicitly considers control delays in the MPC formulation, and considers voltage constraints on the dc grid using ‘soft’ constraints based on slack variables.

This paper provides a number of novel contributions to address the aforementioned issues:

- Firstly, the authors use a Kalman filter to estimate the system state based on a subset of state measurements.
- Secondly, the authors consider dc power losses in the MPC cost function, in addition to minimising frequency deviations in ac areas for AGC, and examine the effect that this has on both the ac and dc side dynamics.
- Finally, the authors examine the effects of extra stochastic sources on the performance of the MPC controller.

The following points as regards the MPC implementation outlined in the paper are relevant. Firstly, as regards the motivation for using MPC here, aside from the ability to explicitly consider the DC voltage constraints, to the best of the authors knowledge there is no trivial way to dynamically consider losses in a DC grid using a simple PI approach. Certainly, as will be seen in this paper, MPC provides a very flexible framework for trading off the frequency regulation and DC losses objectives. Finally, for researchers with an interest in performing further research in the areas outlined in this paper, it is noted that custom modules have been built in the Dome simulation package [21] that allow the methodology outlined in this paper to be applied to various combinations of synchronous machines and VSCs for arbitrary ac/dc grid configurations.

The paper is constructed as follows: the power system modelling is outlined in Section II. MPC and Kalman filtering are presented in Section III. The application of MPC and Kalman filtering for AGC in ac systems connected to MTDC grids is described in Section IV. A case study is then examined in Section V. Finally, conclusions are drawn and some future work is proposed in Section VI.

II. POWER SYSTEM MODELLING FOR CONTROL

The controllers in this paper are used to manipulate the setpoints of both the synchronous ac generators and the frequency regulation scheme of each of the VSCs. Thus the dynamics of these devices are documented in this section.

A standard 6th order dynamic Marconata model is used for simulation and control in this paper to capture the relevant dynamics of the synchronous generators as follows:

$$\dot{\delta} = \Omega_b(\omega - \omega_s), \quad (1)$$

$$2H\dot{\omega} = (\tau_m - \tau_e - D(\omega - \omega_s)), \quad (2)$$

$$T'_{d0}\dot{e}'_d - \tilde{T}''_{d0}\dot{\psi}''_d = -e'_d - (x_d - x'_d)i_d + v_f, \quad (3)$$

$$T'_{q0}\dot{e}'_q - \tilde{T}''_{q0}\dot{\psi}''_q = -e'_q + (x_q - x'_q)i_q, \quad (4)$$

$$T''_{d0}\dot{\psi}''_d = -\psi''_d + e'_d - (x'_d - x_\ell)i_d, \quad (5)$$

$$T''_{q0}\dot{\psi}''_q = -\psi''_q - e'_q - (x'_q - x_\ell)i_q, \quad (6)$$

coupled with the following algebraic equations:

$$\tau_e = \psi_d i_q - \psi_q i_d, \quad (7)$$

$$0 = r_a i_d + \psi_q + v_d, \quad (8)$$

$$0 = r_a i_q + \psi_d + v_q, \quad (9)$$

$$0 = \psi_d + x'_d i_d - \gamma_{d1} e'_q - (1 - \gamma_{d1}) \psi''_d, \quad (10)$$

$$0 = \psi_q + x'_q i_q - \gamma_{q1} e'_d - (1 - \gamma_{q1}) \psi''_q, \quad (11)$$

where δ is the rotor angle (rad), ω is the rotor angular frequency (pu rad/s), τ_m is the mechanical torque (pu Nm), τ_e is the electrical torque (pu Nm), ψ_d and ψ_q represent the d- and q-axis fluxes (pu Wb), the d-axis flux e_q is the transient emf due to field flux linkage (pu V), e'_d is the transient emf due to field flux linkage in the q-axis damper (pu V), i_d and i_q are the d- and q-axis components of stator current (pu A), respectively, v_f is the field voltage (pu V), and ψ''_d and ψ''_q are the sub-transient emfs due to flux linkage in the d- and q-axis dampers (pu V), and \tilde{T}''_{d0} , \tilde{T}''_{q0} , γ_{d1} , and γ_{q1} are time constants and gains as defined in [22]. The parameters associated with the dynamic equations are given in Table I. The remaining relevant algebraic equations associated with this generator type are documented in [22].

The following simplified angular frequency model is presented here to illustrate principles central to frequency regulation which are central to the themes of this paper:

$$2H \frac{d\omega}{dt} = \sum_i^{n_g} p_{gi} + \sum_i^{n_{vsc}} p_{vsci} - p_L - D(\omega - \omega_0) \quad (12)$$

where p_{gi} is the ac power generated in a particular ac area, where there are n_g generators, p_{vsci} are dc injections into that ac area, where there are n_{vsc} dc connected sources, p_L is the load in that area, and D is the damping coefficient. In this paper the ac sources are synchronous generators and the dc sources are VSCs connected to MTDC grids. Thus the regulation of the frequency is a matter of coordinating the synchronous generator and VSC power injections depending on the given load.

TABLE I
SYNCHRONOUS MACHINE PARAMETERS

Variable	Description	Unit
Ω_b	Base angular frequency	rad/s
ω_s	Reference angular frequency	pu (rad/s)
D	Damping coefficient	pu (MW)
H	Inertia constant	MWs/MVA
r_a	armature resistance	pu (Ω)
x_l	Leakage reactance	pu (Ω)
x_d/x_q	d/q-axis synchronous reactance	pu (Ω)
x'_d/x'_q	d/q-axis transient reactance	pu (Ω)
T'_{d0}/T'_{q0}	d/q-axis open circuit transient time constant	s
T''_{d0}/T''_{q0}	d/q-axis open circuit sub-transient time constant	s

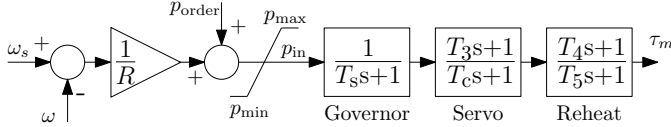


Fig. 1. Turbine Governor control diagram [23].

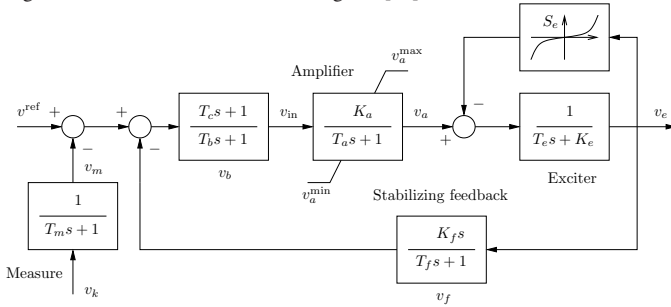


Fig. 2. Automatic Voltage Regulator model [23].

The mechanical power is generated using a turbine governor [23], as given in Fig. 1. This consists of a primary frequency controller, designed to control frequency variations instantaneously based on local frequency measurements, and an additional setpoint p_{ord} which allows the elimination of longer term frequency offsets. The AVR model used with each of the synchronous generators is the IEEE type DC1, given in Fig. 2 [23].

The j^{th} ideal VSC, acting as an interface between an ac grid and the j^{th} MTDC voltage node in a larger dc system, is portrayed in Fig. 3. The following equality applies across the ideal VSC:

$$v_{dcj} \dot{i}_{dcj} = v_{t,aj} \dot{i}_{t,aj} + v_{t,bj} \dot{i}_{t,bj} + v_{t,cj} \dot{i}_{t,cj} \quad (13)$$

where v_{dcj} and i_{dcj} represent the dc voltage and current entering the j^{th} VSC from the dc grid, respectively, $v_{t,aj}$, $v_{t,bj}$, and $v_{t,cj}$ are the sinusoidally varying a, b, and c phase voltages produced on the ac side of the VSC, respectively, and $i_{t,aj}$, $i_{t,bj}$, and $i_{t,cj}$ are the sinusoidally varying a, b, and c phase currents produced on the ac side of the VSC, respectively.

The power balance between the dc and ac sides of the converter is given by:

$$p_{acj} + v_{dcj} \dot{i}_{dcj} - p_{lossj} - \frac{1}{2} C_{dcj} \frac{d(v_{dcj}^2)}{dt} = 0, \quad (14)$$

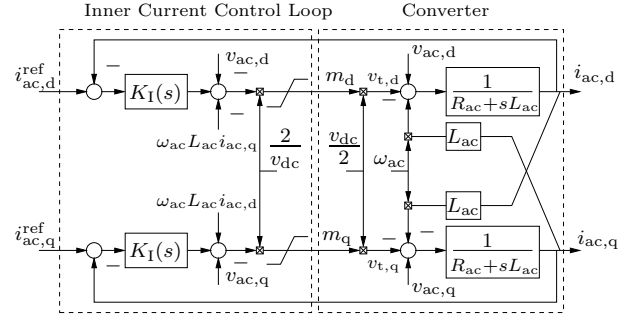


Fig. 3. Block diagram of the VSC inner control loop and converter in dq form [2].

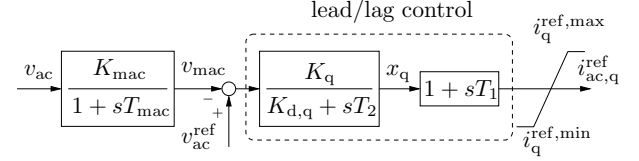


Fig. 4. Block diagram of the VSC outer loop ac voltage control [2].

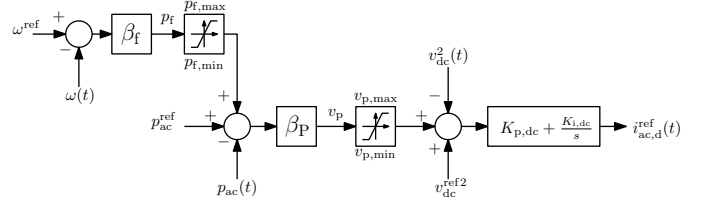


Fig. 5. The primary frequency VSC control loop [2].

where $p_{acj} = \frac{1}{2}(v_{ac,dj} i_{ac,dj} + v_{ac,qj} i_{ac,qj})$, $v_{ac,dj}$ and $v_{ac,qj}$ are ac side voltages represented in the dq rotating frame, and $i_{ac,dj}$ and $i_{ac,qj}$ are ac side currents represented in the dq rotating frame; the $\frac{1}{2} C_{dcj} \frac{d(v_{dcj}^2)}{dt}$ term represents energy variations in the dc side capacitor, where C_{dcj} is the capacitance across the j^{th} VSC's dc voltage node, and $p_{loss} = \frac{3}{2} R_{acj} i_{acj}^2$ is the circuit losses of the converter, where R_{acj} represents the ohmic power loss of the inductor, and $i_{acj}^2 = i_{ac,dj}^2 + i_{ac,qj}^2$. Switching losses in the VSC are ignored here.

The VSC converter dynamics and fast internal VSC control loop of the d and q component currents, $i_{ac,d}$ and $i_{ac,q}$, respectively, are given in Fig. 3. These are modelled in the dq-domain [2]. An outer loop controllers is used to maintain the ac voltage at its scheduled level, as in Fig. 4. Another outer loop controller is used to provide primary frequency regulation from VSCs, as in Fig. 5. This control loops trades off frequency regulation, VSC power setpoint tracking and dc voltage regulation performance.

The voltage dynamics at the j^{th} dc grid node are given by:

$$C_{dcj} \frac{d}{dt} v_{dcj} = \sum_{i=1}^{r_j} R_{dcj\mathcal{N}_j\{i\}}^{-1} (v_{dcj} - v_{dc\mathcal{N}_j\{i\}}), \quad (15)$$

where v_{dcj} is the dc voltage at node j , C_{dcj} is the dc side capacitor, R_{dcjh} is the resistance in the line connecting dc voltage nodes j and h , and \mathcal{N}_j is the indexed set of dc nodes connected to dc node j through a dc line with cardinality r_j .

Traditionally PI controllers have been used to perform AGC. Primary control acts on the local generator frequency signal to regulate the power generated over short ms to s time scales. AGC acts on the seconds to tens of seconds scale using global system information to eliminate long term offsets, which result from local primary control using only proportional gains. Using PI for AGC, the Centre of Inertia (COI) angular frequency signal is sent to a proportional and integral controller to generate $p_{\text{ord}}(t)$ as follows [24]:

$$p_{\text{ord}}(t) = k_I \int_{t=0}^{t=\infty} \omega_{\text{COI}}(t) - \omega_s \, dt \quad (16)$$

where k_I is the integral gain and the centre of inertia angular frequency ω_{COI} is given by:

$$\omega_{\text{COI}}(t) = \frac{1}{H_T} \sum_{i=1}^n H_i \omega_i(t) \quad (17)$$

where there are n synchronous generators in the system and $H_T = \sum_{i=1}^n H_i$.

In order to implement AGC, it is necessary for the TSO to measure $\omega_{\text{COI}}(t)$, calculate the power to inject into the system, and then communicate the various setpoints to each of the generators. Thus, communication delays occur between the measurement of the frequency and the point at which generators receive the updated setpoint changes.

Finally, a scenario in which doubly fed induction generator (DFIG) based wind farms contribute a significant stochastic power injection into the system is considered in the case study. The DFIG wind turbines are described by a variable-speed wind turbine with a 5th-order DFIG model, a double-mass elastic shaft model with tower-shadow effect, a turbine model with continuous pitch control, a cubic maximum power point tracking approximation, a first-order AVR model and a static turbine governor. Wind speeds are modelled using a Weibull distribution [23].

III. MODEL PREDICTIVE CONTROL AND KALMAN FILTERING

A. Model Predictive Control

Model Predictive Control is an optimisation based control technique that uses state-space based predictions in order to form optimal inputs to a system over a prediction horizon. While inputs are calculated over the full prediction horizon, only the input for the first sample step of the prediction horizon is applied to the system, and this process is repeated every sample step.

A discrete-time, linear, time-invariant state-space model for a system is given by

$$\mathbf{x}(k+1) = \mathbf{A}\mathbf{x}(k) + \mathbf{B}\mathbf{u}(k) \quad (18)$$

$$\mathbf{y}(k) = \mathbf{C}\mathbf{x}(k), \quad (19)$$

where $\mathbf{x}(k)$, $\mathbf{u}(k)$, and $\mathbf{y}(k)$ are the states, inputs, and outputs of the system at sample step k , respectively. Matrices \mathbf{A} , \mathbf{B} , and \mathbf{C} are the relevant state-space matrices. An augmented state-space model allows these equations to be framed in terms of $\Delta\mathbf{u}(k)$ and the augmented state $\chi(k)=[\Delta\mathbf{x}^T(k) \ \mathbf{x}^T(k)]^T$

(for a general variable $b(k)$, $\Delta b(k)=b(k)-b(k-1)$, i.e., the Δ operator denotes the change in a variable between sample steps $k-1$ and k), which ensures integral action in the controller. This is given as follows:

$$\chi(k+1) = \underbrace{\begin{bmatrix} \mathbf{A} & \mathbf{0} \\ \mathbf{A} & \mathbf{I} \end{bmatrix}}_{\mathbf{A}} \chi(k) + \underbrace{\begin{bmatrix} \mathbf{B} \\ \mathbf{B} \end{bmatrix}}_{\mathbf{B}} \Delta\mathbf{u}(k) \quad (20)$$

$$\mathbf{y}(k+1) = \underbrace{\begin{bmatrix} \mathbf{0} & \mathbf{C} \end{bmatrix}}_{\mathbf{C}} \chi(k+1). \quad (21)$$

The predicted state $\tilde{\mathbf{x}}(k+1)$ and incremental predicted state $\Delta\tilde{\mathbf{x}}(k+1)$ can be found from these equations, where for a general vector \mathbf{p} , its prediction vector is $\tilde{\mathbf{p}}(k)=[\mathbf{p}^T(k) \dots \mathbf{p}^T(k+H-1)]^T$, where H is called the prediction horizon for the system [8]. This results in the following state prediction matrices:

$$\tilde{\chi}(k+1) = \tilde{\mathbf{A}}\tilde{\chi}(k) + \tilde{\mathbf{B}}\Delta\tilde{\mathbf{u}}(k). \quad (22)$$

The tilde notation is used with the matrices here to denote that they are prediction matrices.

It should be noted that once these predictions have been formulated it is straightforward to consider the case where there is control communication delays. If there is a delay of ς samples, then $\Delta\mathbf{u}(k), \dots, \Delta\mathbf{u}(k+\varsigma-1)$ are considered constant at the values that they were calculated at in sample steps $k-\varsigma, \dots, k-1$, and inputs variables $\Delta\mathbf{u}(k+\varsigma), \dots, \Delta\mathbf{u}(k+H-1)$ are optimised for. Thus $\tilde{\mathbf{B}}$ in (22) can be separated into those elements that correspond to the constant part of the input vector and the part that corresponds to the subset of the predicted inputs that are to be optimised for.

MPC problems are constructed to fulfill control objectives for a system based on knowledge of $\mathbf{x}(k)$. A cost function, $J(\chi(k), \Delta\tilde{\mathbf{u}}(k))$ (which will henceforth be denoted by $J(k)$), is designed so as to embody the system's objectives. Typically this cost function is quadratic in $\Delta\tilde{\mathbf{u}}$. The quadratic function used in this paper will be discussed in Section IV. The optimal choice of controls can be found by solving the following optimisation problem:

$$\begin{aligned} \Delta\tilde{\mathbf{u}}^*(k) &= \min_{\Delta\tilde{\mathbf{u}}(k)} J(k), \\ \text{s.t.} \quad \mathbf{A}\Delta\tilde{\mathbf{u}}(k) &\leq \mathbf{b}, \end{aligned} \quad (23)$$

where a superscripted $*$ denotes the optimum value of a variable, and \mathbf{A} and \mathbf{b} represent inequality constraints in the control problem.

If there are feasibility issues associated with the inequality constraints, due to model uncertainties, it is possible to reframe the inequality constraints as 'soft' constraints by minimising the infinite norm of an additional slack variable, ϵ . Feasibility is thus maintained by seeking to minimise the value of ϵ in order to maintain the desired inequality constraint. The following formulation of the problem achieves this objective [8]:

$$\begin{aligned} \Delta\tilde{\mathbf{u}}^*(k) &= \min_{\Delta\tilde{\mathbf{u}}(k), \epsilon} J(k) + \rho\epsilon, \\ \text{s.t.} \quad \mathbf{A}\Delta\tilde{\mathbf{u}}(k) &\leq \mathbf{b} + \mathbf{1}\epsilon, \\ &\epsilon \geq 0, \end{aligned} \quad (24)$$

where $\mathbf{1}$ is a vector of ones with the same dimensions as \mathbf{b} . Once the predicted inputs from MPC have been computed, the input at the start of the horizon $\mathbf{u}(k)$ is applied to the system and this process is repeated each sample step.

B. State estimation using Kalman filtering

When it is undesirable, un-economic or impossible to measure certain states for MPC, a Kalman filter can be used to estimate them. Kalman filters allow a maximum likelihood estimate of states to be formed provided the noise associated with both the states and the output measurements are normally distributed about the mean [25]. We will henceforth assume that Kalman filtering is used with MPC for the rest of the paper to estimate unmeasured states.

Consider the following state-space and output measurement equations,

$$\mathbf{x}_\epsilon(k+1) = \mathbf{A}\mathbf{x}_\epsilon(k) + \mathbf{B}\mathbf{u}(k) + \mathbf{w}(k), \quad (25)$$

$$\mathbf{z}(k) = \mathbf{y}(k) + \mathbf{v}(k) = \mathbf{C}_\epsilon\mathbf{x}_\epsilon(k) + \mathbf{v}(k), \quad (26)$$

where $\mathbf{x}_\epsilon(k)$ is the state estimate, the state noise uncertainty $\mathbf{w}(k) \sim \mathcal{N}(0, \boldsymbol{\sigma}_w)$, $\boldsymbol{\sigma}_w$ is the variance at sample step k of the state noise uncertainty, the output measurement noise uncertainty $\mathbf{v}(k) \sim \mathcal{N}(0, \boldsymbol{\sigma}_v)$, $\boldsymbol{\sigma}_v$ is the variance at sample step k of the output measurement, and \mathbf{C}_ϵ is the Kalman state output matrix. A Kalman filter effectively merges the predicted state measurement based on (18) with the new output measurement given by (26), to give an update of the new state estimate and the associated state covariance matrix $\mathbf{P}(k)$ as follows [26]:

$$\mathbf{P}^*(k) = \mathbf{A}_\epsilon\mathbf{P}(k)\mathbf{A}_\epsilon^T + \boldsymbol{\sigma}_w, \quad (27)$$

$$\mathbf{K}(k+1) = \mathbf{P}^*(k)\mathbf{C}_\epsilon^T(\mathbf{C}_\epsilon\mathbf{P}^*(k)\mathbf{C}_\epsilon^T + \boldsymbol{\sigma}_v)^{-1}, \quad (28)$$

$$\mathbf{x}_\epsilon(k+1) = (\mathbf{I} - \mathbf{K}(k+1)\mathbf{C}_\epsilon)(\mathbf{A}_\epsilon\mathbf{x}_\epsilon(k) + \mathbf{B}_\epsilon\mathbf{u}(k)) + \mathbf{K}(k+1)\mathbf{z}(k), \quad (29)$$

$$\mathbf{P}(k+1) = (\mathbf{I} - \mathbf{K}(k+1)\mathbf{C}_\epsilon)\mathbf{P}^*(k), \quad (30)$$

where $\mathbf{P}^*(k+1)$ is the covariance as predicted by (18). The Kalman gain matrix \mathbf{K} is chosen on the basis of the error covariance and noise statistics at sample step $k-1$, so as to minimise the variance of the next estimate. When the Kalman filter is used with MPC $\mathbf{x}(k) = \mathbf{x}_\epsilon(k)$.

IV. FORMULATING MPC FOR AGC IN MTDC GRIDS

A. Deriving the state-space MPC model from the semi-implicit DAE.

The first step involved in designing the MPC is to derive a suitable state-space model that considers the dynamics of the system at the time-scales of interest. The authors have developed custom functionality for the ‘Dome’ power systems simulation package [21] that automates the process whereby the state-space matrix used for control is constructed. This process will now be described.

The dynamic behaviour of electrical power systems can be described using a nonlinear semi-implicit differential algebraic equation (SIDAE) [22]:

$$\begin{bmatrix} \mathbf{T}_{nl} & \mathbf{0} \\ \mathbf{R}_{nl} & \mathbf{0} \end{bmatrix} \begin{bmatrix} \dot{\mathbf{x}}_{nl} \\ \mathbf{0} \end{bmatrix} = \begin{bmatrix} \mathbf{f}(\mathbf{x}_{nl}, \mathbf{y}_{nl}) \\ \mathbf{g}(\mathbf{x}_{nl}, \mathbf{y}_{nl}) \end{bmatrix} \quad (31)$$

where \mathbf{x}_{nl} denotes the dynamic states of the nonlinear power system, \mathbf{y} are the algebraic states, and in general \mathbf{T}_{nl} and \mathbf{R}_{nl} are time-variant, non-diagonal and non-full rank. The matrix $\mathbf{0}$ denotes a matrix of zeros. Equations \mathbf{f}_{nl} are the explicit part of the nonlinear differential equations and \mathbf{g}_{nl} are the explicit part of the nonlinear algebraic equations. The first step to deriving the state-space matrices used by MPC is to linearise (31) giving:

$$\begin{bmatrix} \hat{\mathbf{T}} & \mathbf{0} \\ \hat{\mathbf{R}} & \mathbf{0} \end{bmatrix} \begin{bmatrix} \dot{\mathbf{x}}_{nl} \\ \mathbf{0} \end{bmatrix} = \begin{bmatrix} \mathbf{f}_x & \mathbf{f}_y \\ \mathbf{g}_x & \mathbf{g}_y \end{bmatrix} \begin{bmatrix} \mathbf{x}_l \\ \mathbf{y} \end{bmatrix}, \quad (32)$$

where $\hat{\mathbf{T}}$, $\hat{\mathbf{R}}$, \mathbf{f}_x , \mathbf{f}_y , \mathbf{g}_x , and \mathbf{g}_y are the linearisations of \mathbf{T}_{nl} , \mathbf{R}_{nl} , $\mathbf{f}(\mathbf{x}_{nl}, \mathbf{y})$, and $\mathbf{g}(\mathbf{x}_{nl}, \mathbf{y})$ with respect to the \mathbf{x}_{nl} and \mathbf{y}_0 at linearisation point $(\mathbf{x}_{nl0}, \mathbf{y}_0)$. The linearised state variables are given by $\mathbf{x}_l = \mathbf{x}_{nl} - \mathbf{x}_{nl0}$ and the linearised algebraic variables are given by $\mathbf{y} = \mathbf{y}_{nl} - \mathbf{y}_0$. At this stage (32) represents a linearisation of the entire simulated system. The following paragraphs show how the state-space used for control is extracted from this linearised semi-implicit model of the system.

The MPC typically has access to the models and inputs of a subset of devices for the purposes of control, and so these first must be separated from the remaining elements in the system. The dynamic states, the equations relevant to the MPC, and the inputs are expressed separately from the remaining system states, algebraic variables, and dynamic equations as follows:

$$\begin{bmatrix} \mathbf{T} & \mathbf{T}_{xg} & \mathbf{0} & \mathbf{0} \\ \mathbf{T}_{rxd} & \mathbf{T}_{rxg} & \mathbf{0} & \mathbf{0} \\ \mathbf{R} & \mathbf{R}_{xg} & \mathbf{0} & \mathbf{0} \\ \mathbf{R}_{rxd} & \mathbf{R}_{rxg} & \mathbf{0} & \mathbf{0} \end{bmatrix} \begin{bmatrix} \dot{\mathbf{x}}_d \\ \dot{\mathbf{x}}_g \\ \mathbf{0} \\ \mathbf{0} \end{bmatrix} = \begin{bmatrix} \mathbf{f}_{xd} & \mathbf{f}_{xg} & \mathbf{f}_y & \mathbf{f}_u \\ \mathbf{f}_{rxd} & \mathbf{f}_{rxg} & \mathbf{f}_{ry} & \mathbf{f}_{ru} \\ \mathbf{g}_x & \mathbf{g}_{xg} & \mathbf{g}_y & \mathbf{g}_u \\ \mathbf{g}_{rxd} & \mathbf{g}_{rxg} & \mathbf{g}_{ry} & \mathbf{g}_{ru} \end{bmatrix} \begin{bmatrix} \mathbf{x}_d \\ \mathbf{x}_g \\ \mathbf{y}_r \\ \mathbf{u} \end{bmatrix} \quad (33)$$

Here \mathbf{x}_d denotes the dynamic states which the MPC has access to for use in its model. The remaining states which are not used by MPC are denoted by \mathbf{x}_g . The control inputs, \mathbf{u} , used for AGC are considered as algebraic variables. Thus, these are separated from the remaining algebraic variables \mathbf{y}_r . The first and third rows of (33) (the rows corresponding to \mathbf{T} and \mathbf{R}) denote the rows of dynamic and algebraic equations which the MPC has access to. The second and fourth rows of equations are used in the simulation but are not known by the MPC. As it is assumed that \mathbf{x}_g is unknown to the MPC, then the MPC model ignores the effects of matrices \mathbf{f}_{xg} and \mathbf{g}_{xg} .

This leaves the following two equations which can be used to form the state-space representation:

$$\begin{bmatrix} \mathbf{T} & \mathbf{0} \\ \mathbf{R} & \mathbf{0} \end{bmatrix} \begin{bmatrix} \dot{\mathbf{x}}_d \\ \mathbf{0} \end{bmatrix} = \begin{bmatrix} \mathbf{f}_x & \mathbf{f}_u & \mathbf{f}_y \\ \mathbf{g}_x & \mathbf{g}_u & \mathbf{g}_y \end{bmatrix} \begin{bmatrix} \mathbf{x}_d \\ \mathbf{u} \\ \mathbf{y}_r \end{bmatrix} \quad (34)$$

By rearranging the second row of (34) to give \mathbf{y}_r in terms of \mathbf{x}_d , \mathbf{u} , and $\dot{\mathbf{x}}_d$, and substituting this value of \mathbf{y}_r into the first row of (34), the state-space representation $\dot{\mathbf{x}}_d = \mathbf{A}_d\mathbf{x}_d + \mathbf{B}_d\mathbf{u}$ can be found where $\mathbf{A}_d = (\mathbf{T} - \mathbf{f}_y\mathbf{g}_y^{-1}\mathbf{R}_x)^{-1}(\mathbf{f}_x - \mathbf{f}_y\mathbf{g}_y^{-1}\mathbf{g}_x)$ and $\mathbf{B}_d = (\mathbf{T} - \mathbf{f}_y\mathbf{g}_y^{-1}\mathbf{g}_x)^{-1}(\mathbf{f}_u - \mathbf{f}_y\mathbf{g}_y^{-1}\mathbf{g}_u)$.

Often the dynamics of certain states of the MPC state-space model will occur on time-scales which are relatively fast in comparison to the dynamics of the other states. By considering these variables as algebraic in the MPC state-space model, it allows larger sample times to be used for the discretisation of the model. As a result the MPC can predict the system response further into the future for the same prediction horizon. This is conducted as follows. The dynamic states are divided into those states whose dynamics are maintained, \mathbf{x} , and those whose time constants are to be set to zero \mathbf{x}_0 . Setting the time constants associated with \mathbf{x}_0 to zero gives the following:

$$\begin{bmatrix} \dot{\mathbf{x}} \\ \mathbf{0} \end{bmatrix} = \begin{bmatrix} \mathbf{A}_d \\ \mathbf{A}_{21} & \mathbf{A}_{22} \end{bmatrix} \begin{bmatrix} \mathbf{x} \\ \mathbf{x}_0 \end{bmatrix} + \begin{bmatrix} \mathbf{B}_d \\ \mathbf{B}_2 \end{bmatrix} \mathbf{u} \quad (35)$$

Then by expressing \mathbf{x}_0 in terms of \mathbf{x} and \mathbf{u} using the second row of the (35) the state-space representation to be used for the control of the system, $\dot{\mathbf{x}}(t) = \mathbf{A}\mathbf{x}(t) + \mathbf{B}\mathbf{u}(t)$ is found where $\mathbf{A} = \mathbf{A}_{11} - \mathbf{A}_{12}\mathbf{A}_{22}^{-1}\mathbf{A}_{21}$ and $\mathbf{B} = \mathbf{B}_1 - \mathbf{A}_{12}\mathbf{A}_{22}^{-1}\mathbf{B}_2$. Having discussed how the MPC state-space is formed from the nonlinear SIDAE, the constitution of the state-space model and the construction of the MPC cost function and constraints are now outlined.

B. MPC state-space description and design.

In this paper, all the dynamics associated with the synchronous machines, the VSCs, and the various controllers associated with these devices, as described in Section II constitute the control model that the MPC has access to for constructing the state-space model. Many of the dynamics of the synchronous machines and VSCs occur on time scales which are significantly faster than those of interest for the MPC. Thus, it is desirable to set the time constants associated with the following dynamic states to zero; with regard to the synchronous machines the time constants associated with the voltage and flux dynamics of variables e'_d , e'_q , Ψ'_d , and Ψ'_q , and the time constants associated with the states of the Automatic Voltage Regulators; with regard to the VSCs, the time constants associated with the VSC inner loop current dynamics, the inner loop current controller dynamics, and those associated with the VSC ac voltage controller. Thus, the dynamic state is given by $\mathbf{x} = [\mathbf{x}_v^T, \mathbf{x}_\delta^T, \mathbf{x}_\omega^T, \mathbf{x}_{tg}^T, \mathbf{x}_{vscf}^T]^T$, where $\mathbf{x}_v = [x_{v1}, \dots, x_{vn_v}] = [v_{dc1} - v_{dc10}, \dots, v_{dcn_v} - v_{dcn_v0}]^T$, with n_v representing the number of VSC connected voltage nodes in the dc grid, $\mathbf{x}_\delta = [\delta_1 - \delta_{10}, \dots, \delta_{n_g} - \delta_{n_g0}]^T$, $\mathbf{x}_\omega = [\omega_1 - \omega_{10}, \dots, \omega_{n_g} - \omega_{n_g0}]^T$, with n_g representing the number of synchronous generators in the system under MPC control, and \mathbf{x}_{tg} and \mathbf{x}_{vscf} represent the deviation of the states associated with the turbine governor and VSC outer loop frequency controller from their linearisation points, respectively. In all the above, and in the remainder of the paper, the 0 subscript denotes the linearisation point of that particular variable. The input vector to the system is given by $\mathbf{u} = [p_{ord1}^{tg} - p_{ord10}^{tg}, \dots, p_{ordn_g}^{tg} - p_{ordn_g0}^{tg}, p_{ord1}^{vsc} - p_{ord10}^{vsc}, \dots, p_{ordn_v}^{vsc} - p_{ordn_v0}^{vsc}]^T$, where p_{ordi}^{vsc} is the setpoint sent

to the i^{th} turbine generator, and p_{ordi}^{vsc} is the setpoint sent to the i^{th} VSC primary frequency regulator.

It is necessary to design the MPC such that the setpoints of the ac machines and VSCs are manipulated so as to minimise predicted frequency deviations in the ac areas, while minimising losses on the dc grid, and maintaining dc voltages within desired bounds. Thus, the following quadratic equation is proposed:

$$J(k) = \tilde{\mathbf{x}}_\omega^T \mathbf{Q}_\omega \tilde{\mathbf{x}} + \tilde{\mathbf{x}}_v^T \tilde{\mathbf{G}} \tilde{\mathbf{x}}_v + \Delta \tilde{\mathbf{u}}^T \mathbf{Q}_u \Delta \tilde{\mathbf{u}} \quad (36)$$

where weighting matrices $\mathbf{Q}_\omega = \text{diag}(q_\omega, \dots, q_\omega)$, $\mathbf{Q}_l = \text{diag}(q_l, \dots, q_l)$, and $\mathbf{Q}_u = \text{diag}(q_u, \dots, q_u)$, determine the relative importance of minimising the frequency error, the dc power losses and the changes in inputs from sample to sample, respectively, q_ω , q_l , and q_u are tuning constants for these matrices, and the (k) the $(k+1)$ dependencies are dropped from $\tilde{\mathbf{x}}_\omega(k+1)$, $\tilde{\mathbf{x}}_v(k+1)$, and $\Delta \mathbf{u}(k)$ for compactness. The first cost term of (36) is related to the minimisation of the frequency error. The final term of (36) is a stabilising term which provides robustness against uncertainty by discouraging changes in the input from sample to sample.

Losses in the DC grid are given as follows:

$$\begin{aligned} \mathbf{v}^T \mathbf{G} \mathbf{v} &= P_{dc1} + \dots + P_{n_v} \\ &= v_{dc1} \sum_{i=1}^{r_1} R_{dc1N_1\{i\}}^{-1} (v_{dc1} - v_{dcN_1\{i\}}) + \dots \\ &\quad + v_{dcn_v} \sum_{i=1}^{r_{n_v}} R_{dcn_vN_{n_v}\{i\}}^{-1} (v_{dcn_v} - v_{dcN_{n_v}\{i\}}) \end{aligned} \quad (37)$$

where the $(k+1)$ dependency has been omitted from the v_{dc} and P_{dc} variables for compactness, and $\mathbf{v} = [v_{dc1}, \dots, v_{dcn_v}]^T$ [16]. Here, conductances are positioned in \mathbf{G} such that the equality in (37) holds, and $\tilde{\mathbf{G}} = \text{diag}(\mathbf{G}, \dots, \mathbf{G})$. The cost, $\tilde{\mathbf{x}}_v^T \tilde{\mathbf{G}} \tilde{\mathbf{x}}_v$, in (37) does not explicitly minimise the total DC losses, but does provide a quantity to the MPC that is representative of the predicted losses on the DC network about the linearisation point \mathbf{v}_0 . It is noted that while the frequency/dc losses trade-off is focused on in this paper, MPC can account for a range of objectives with relation to dc networks. The authors refer to [18] as an example.

It is desirable to regulate the dc voltages within bounds using slack constraints in order to avoid the possibility of infeasibility due to uncertainties related to the dc grid or approximations in the MPC model due to linearisation of the nonlinear system model. Thus the following slack inequality constraint is applied:

$$\begin{bmatrix} \mathbf{I}_H \\ -\mathbf{I}_H \end{bmatrix} \tilde{\mathbf{x}}_{vi} \leq \begin{bmatrix} \mathbf{x}_{v,maxi} \\ -\mathbf{x}_{v,mini} \end{bmatrix} + \begin{bmatrix} \mathbf{1} \\ \mathbf{1} \end{bmatrix} \epsilon_i, \quad \text{for } i = 1, \dots, n_v, \quad (38)$$

where \mathbf{I}_H is a $H \times H$ identity matrix, $\mathbf{x}_{v,maxi} = [x_{v,maxi}, \dots, x_{v,maxi}]^T$ and $\mathbf{x}_{v,mini} = [x_{v,mini}, \dots, x_{v,mini}]^T$, with $x_{v,maxi}$ and $x_{v,mini}$ denoting the desired upper and lower bounds for x_{vi} , respectively, and ϵ_i is the slack variable associated with the i^{th} dc voltage node. Having formulated the cost function, as in (36), and the slack constraint as above, the MPC problem can then be solved, as in (24).

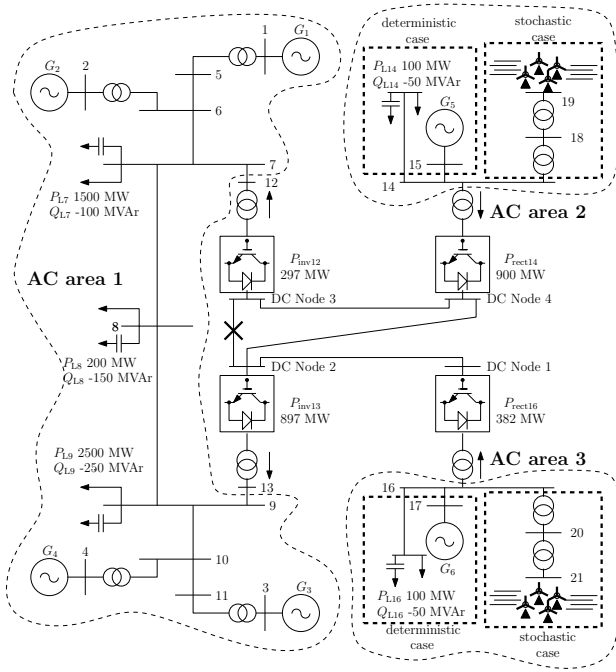


Fig. 6. Case study grid. For the deterministic case the wind power input is zero.

Finally, it is necessary to use the Kalman filter in order to estimate the state $x(k)$. The following measurement vector allows for estimation of this state, $z = [\delta_1, \omega_1, \dots, \delta_{n_g}, \omega_{n_g}, v_{dc1}, \dots, v_{dcn_v}]$. The Kalman filter can then be used to estimate the system state, as in (27)-(30).

The authors note here that customised integrated functionality has been constructed in the Dome [21] simulation system, which automates the process of constructing the state-space, MPC, and Kalman filter for the system. Once the user of the software has initially specified the generators and VSCs to be controlled using MPC, and the various tuning parameters and constraints to be applied, the software automates the rest of the process of constructing and applying the control. It is hoped that this will help improve the efficiency with which MPC can be applied to ac/dc based systems in future. In the following section the MPC based AGC will be applied to a MTDC testbed.

V. CASE STUDY

A. Simulation details

The authors considered an augmented version of the testbed previously utilised in [2], as shown in Fig. 6, including both extra loads and DFIG-based farms. Two cases are considered for simulation. The first considers a deterministic case where areas 2 and 3 consist of a synchronous generator which serves a local load and sends energy through the VSCs to ac area 1. In the second case, which considers stochastic power production, areas 2 and 3 consist of 2 DFIG based wind farms that provide 900 MW and 300 MW to ac area 1, respectively.

The simulation was built using the Dome software package [21]. The base power is given by $S_{base} = 100$ MW, base voltage $V_{base} = 470$ kV, and base frequency $f_{ac} = 50$ Hz.

TABLE II
GENERATOR PARAMETERS

Generator	1	2	3	4	5	6
P_m^0 (pu MW)	7.02	7.02	10.09	7.02	10.09	4.84
M (s)	13	13	12.35	12.35	12.35	12.35
R	0.05	0.05	0.05	0.05	0.05	0.05

TABLE III
VSC PARAMETERS

VSC	1	2	3	4
v_{dc}^0 (pu kV)	1	0.986	0.988	1.09
β_f (pu MW)	1	1	1	1
β_P (s)	0.1	0.5	0.5	0.1

The generator values are given as in Table II, where P_m^0 is the initial power output in pu of generator j , and M gives the inertia of each generator in s. VSC proportional gain parameters and initial dc voltages at each of the VSCs v_{dc}^0 are given in Table III for the deterministic case. Each VSC uses a value of $K_{p,dc} = 1$ and $K_{i,dc} = 1$. These proportional and integral gains result in stable behaviour after a fault but also result in an underdamped response. These gains are chosen to highlight the ability of the various AGC strategies to improve systemwide damping.

The HVDC lines are modelled as asymmetric monopolar lines [2] with shunt capacitances $C_{dcj} = 0.4$ mF for $j = 1 \dots n_v$, and the following dc resistance value on the dc lines: $R_{12} = 8 \Omega$, $R_{24} = 70 \Omega$, $R_{23} = 1.5 \Omega$, $R_{34} = 45 \Omega$. Each of the VSCs are equipped with a local voltage controller and the outer frequency droop control loop shown in Fig. 5. For the stochastic case the DFIGs provide the power from AC areas 2 and 3 so as to contribute a significant stochastic power contribution to the system.

In the stochastic case, the same parameters in Table III are used except $\beta_{f1} = 0$, $\beta_{f4} = 0$, $\beta_{P1} = 0.5$, $\beta_{P4} = 0.5$, where β_{fi} and β_{Pi} denote the frequency and ac power regulation gains associated with the primary controller of the VSC connected to DC node i . In this scenario, it is assumed that the wind farms provide power to serve the regulation of frequency in ac area 1. Thus, the frequency gains are set to zero as VSCs 1 and 4 are not used for local frequency regulation. However, the p_{ord} signals for the VSCs at DC nodes 1 and 4 are controlled using AGC in order to help regulate ω_{coi1} .

The MPC and Kalman filter parameters used in simulations are given in the following. A sample time of 0.1 s was used for the discretisation and a prediction horizon of $2.5 + d_c$ s was used, where d_c constitutes the control communication delay time in s. The weights used in the weighting matrices are given by $q_\omega = 5$, $q_l = 1$, $q_u = 0.1$, and the weight used for the slack constraint $\rho = 0.01$. For the PI-based AGC controllers, the integral gains for the synchronous generators and VSC setpoint control loops are set to $k_I = 10$. These controller weights were chosen using trial and error in order to give a stable and damped response. The tuning of these variables can significantly impact the performance of the controller. The dc voltages limits are given by $v_{maxi} = v_{dci}^0 + 0.1$ pu and $v_{mini} = v_{dci}^0 - 0.1$ pu, for $i = 1, \dots, 4$. The Kalman filter was tuned such that $\sigma_v = 0.01$ and $\sigma_w = 0.001$ which gave accurate state tracking. The loss of the dc line between nodes 2 and

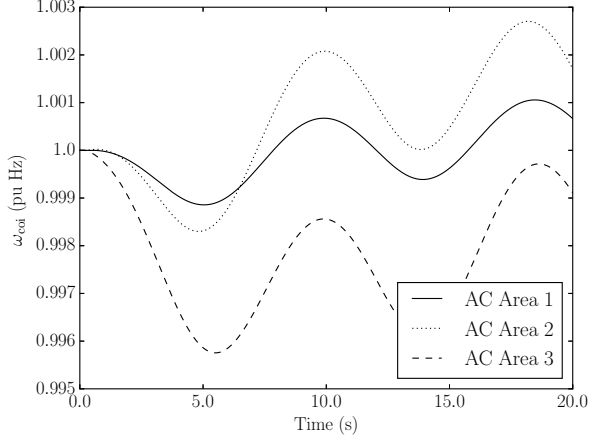


Fig. 7. First 20 s of PI based simulation. Illustrates effect of dc line loss.

3 was considered in simulations. This results in a significant disturbance for both the ac and dc systems and represents considerable model uncertainty from the point of view of the MPC controllers. The results will now be discussed.

B. Results

First, the simulations were run for the deterministic case, where there is no contribution from the DFIGs. Two control communication delays were considered, 3 s and 5 s, with 3 s representing a realistic communication delay between the TSO and VSCs and generators, and 5 s included to illustrate the effect of a longer delay time on the control performance. The authors considered 4 different control scenarios for these simulations; an unconstrained MPC that considers both frequency error and dc loss minimisation (MPC LM), a MPC that considers frequency error and dc loss minimisation and uses slack variable to enforce soft dc voltage constraints (MPC LMS), an MPC that only considers frequency error minimisation but also uses slack variables to regulate the dc node voltages (MPC Slack), and finally a PI controller that provides integral gain based AGC control for the VSC and generator setpoints to minimise frequency errors (PI).

The results for the 3 s delay scenario can be seen in Figs. 8-13, which show the frequency responses in each of the ac areas, the dc voltage responses, and the overall dc power losses in the grid, respectively. Figure 7 illustrates the initial impact of the dc line loss on the AC areas for the PI case. It can be seen in Figs. 8-13, that the MPC LM cases provide the best frequency regulation and dc loss minimisation performance, while providing significantly better damping than the other algorithms. The MPC slack controller provides improved frequency regulation versus the PI controller, while regulating the dc voltage within bounds. However, it provides a very poorly damped frequency response, as does the PI controller.

The authors note here issues regarding the use of slack inequality constraints for the MPC LMS case. Figure 12 shows how the need to satisfy the constraints on v_{dc3} at around 150 s induces a frequency deviation as it seeks to satisfy the voltage constraints and minimise the dc power losses.

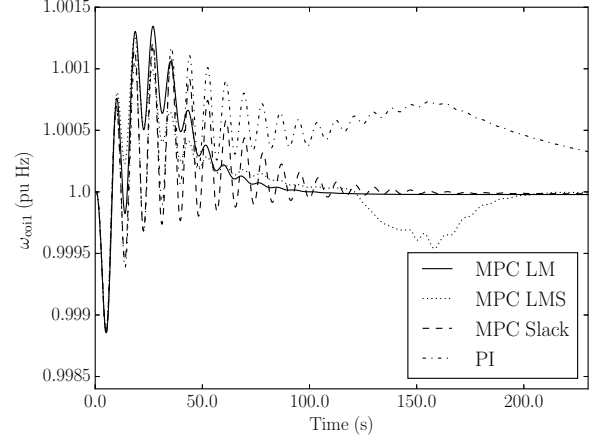


Fig. 8. COI frequency in area 1 for 3 s delay. Deterministic case.

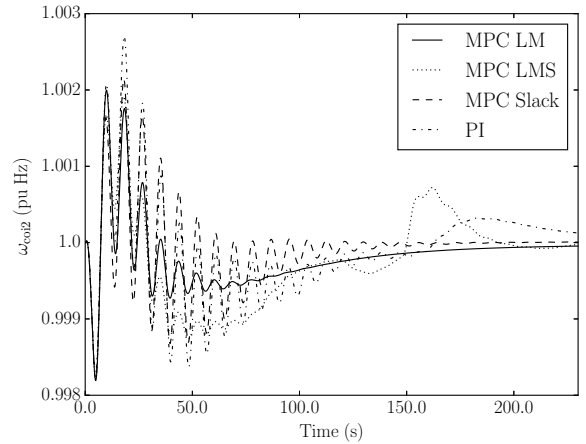


Fig. 9. COI frequency in area 2 for 3 s delay. Deterministic case.

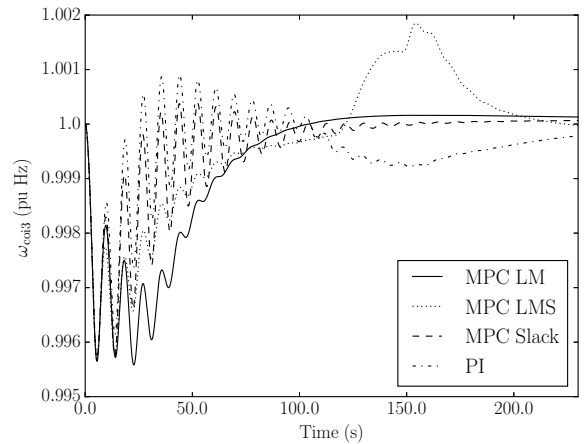


Fig. 10. COI frequency in area 3 for 3 s delay. Deterministic case.

Comparing v_{dc3} for the MPC and LM cases, it can be seen, that the MPC LMS reduces the voltage oscillations for the first 100 s in order to satisfy the slack voltage constraints. This, however, results in a voltage drift towards the lower voltage limit. Looking at Figs. 12 and 13, it can be seen that the MPC LMS is capable of both returning v_{dc3} within the desired

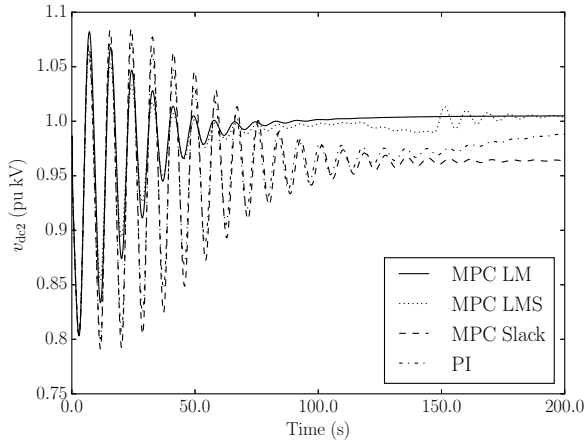


Fig. 11. DC grid voltages at dc node 3 with 3 s delay. Deterministic case.

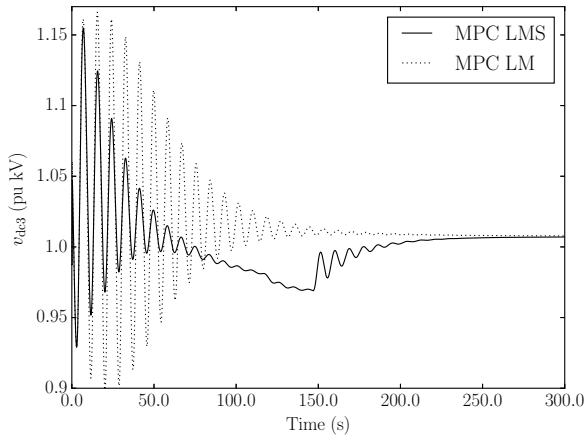


Fig. 12. DC grid voltages at dc node 3 with 3 s delay. Deterministic case.

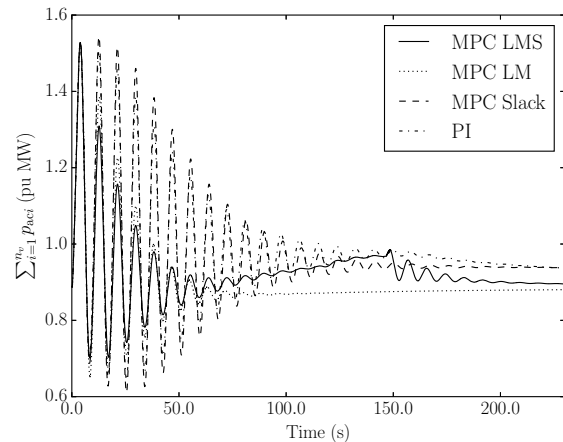


Fig. 13. DC grid power losses with 3 s delay. Deterministic case.

bounds and reducing the DC losses. The trade off, however, is the introduction of frequency deviations in each of the AC areas, as can be seen in Figs. 8-10. The MPC LMS is forced into this situation, unlike the MPC LM, because it suppresses some of the earlier voltage deviations. Thus, for practitioners who may use this algorithm, careful consideration would need

to be given to the introduction of slack voltage constraints, as it may result in undesirable frequency deviations, due to voltage regulation issues on the DC grid. However, this is a very nice illustration of how MPC is capable of handling the various system objectives in an intelligent way. It is only at the 150 s mark that, having damped much of the larger initial frequency, that it then focuses its ‘attention’ on minimising the DC grid losses, all the while maintaining the DC voltages within bounds. With SISO PI control approaches, attaining this level of coordination, while maintaining a high system-wide performance, is certainly more difficult to achieve.

The results of the deterministic case with a 5 s communication delay can be seen in Figs. 14 and 15. The same hierarchy of control performance as was seen for the 3 s case occurs in this case too. However, it is observed that this longer delay results in an increasingly underdamped response from the MPC controllers, as can be seen in Fig. 14. This is likely because of the disparity between the linear control model and the nonlinear system when using a longer prediction horizon. The linear and nonlinear models match closely up to about 3 s but begin to deviate for longer horizons, as can be seen for the step test in Fig. 16. These disparities could thus result in the MPC ‘seeing’ larger errors further into the future, and thus increasing the suboptimality of the input applied to the system, as opposed to the case for a shorter horizon. Therefore when considering these linear MPC controllers, it is important to consider the accuracy of predictions past a certain prediction horizon.

The results from the stochastic case are given in Figs. 17-19. Given the aforementioned issues as regards the MPC LMS algorithm, the authors chose to compare the unconstrained MPC LM algorithm against the PI controller for a communication delay of 3 s. It can be seen in each case that the MPC is robust to the extra noise uncertainty due to the wind, providing reduced dc losses, improved frequency error minimisation and better frequency damping than the PI case.

Finally, the effectiveness of the Kalman filter is evaluated for this stochastic scenario. It should be noted that the noise injected from the wind is based on a non-normal Weibull distribution. As Kalman filters assume normal noise distributions, it is of interest to investigate the state estimation performance under non-normal noise uncertainty, and parameter uncertainty in the dc grid. Fig. 20 shows the state estimate of one of the internal VSC voltage regulation loops. It can be seen here that the Kalman filter provides a highly accurate state estimate here of this unmeasured state, as it does for the other estimated state variables.

C. Penalising DC setpoint deviations

Typically point-to-point HVDC controllers are designed so as to regulate DC line voltages such that the scheduled DC power is maintained. Thus it is of interest to investigate the performance of the controllers when deviations from the scheduled p_{ac}^{ref} values, p_{ac0}^{ref} , are penalised.

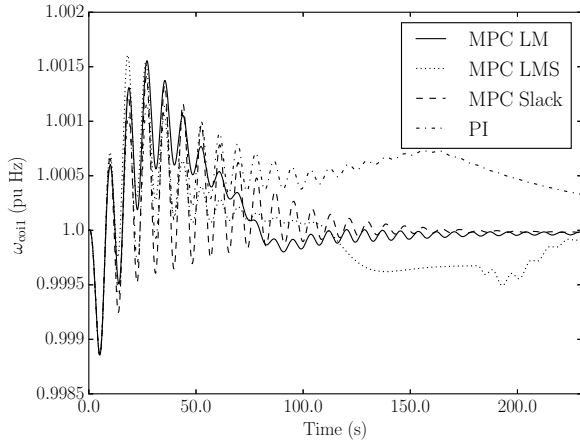


Fig. 14. COI frequency in area 1 for 5 s delay. Deterministic case.

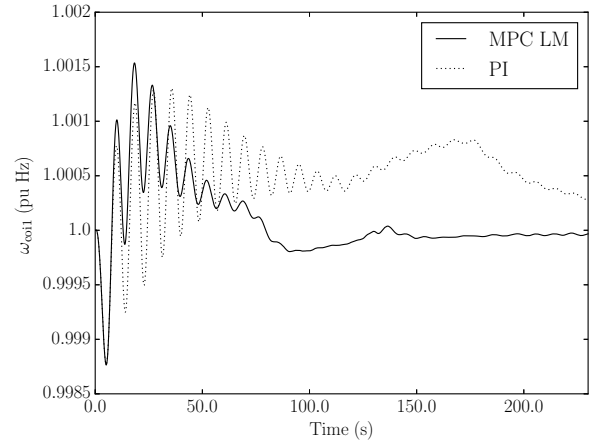


Fig. 17. COI frequency in area 1 for 3 s delay. Stochastic wind case.

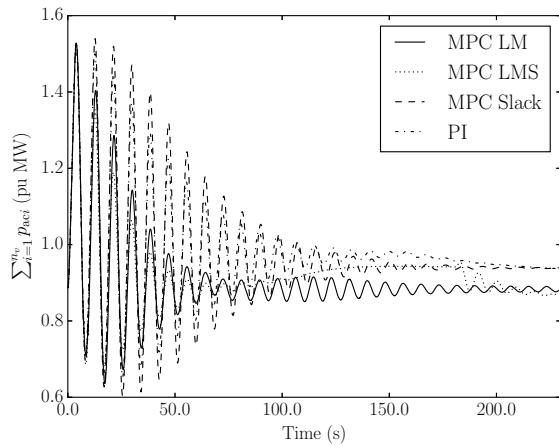


Fig. 15. DC grid power losses with 5 s delay. Deterministic case.

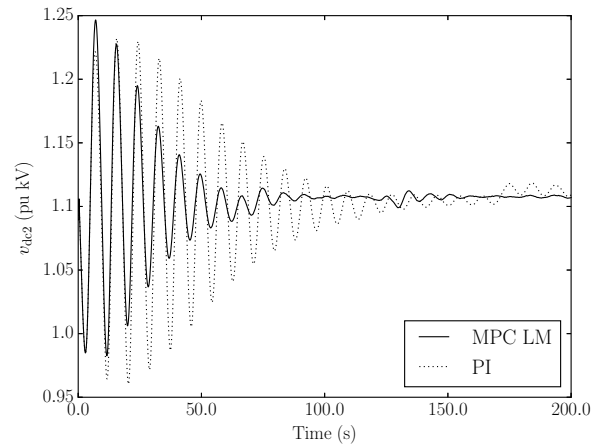


Fig. 18. DC grid voltages at dc node 2 with 3 s delay. Stochastic wind case.

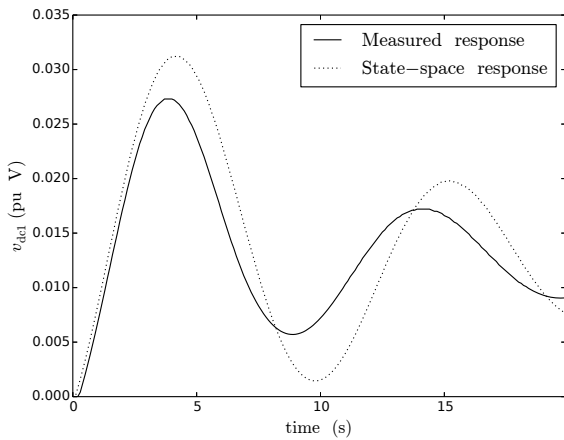


Fig. 16. Step test comparison between nonlinear and linear models.

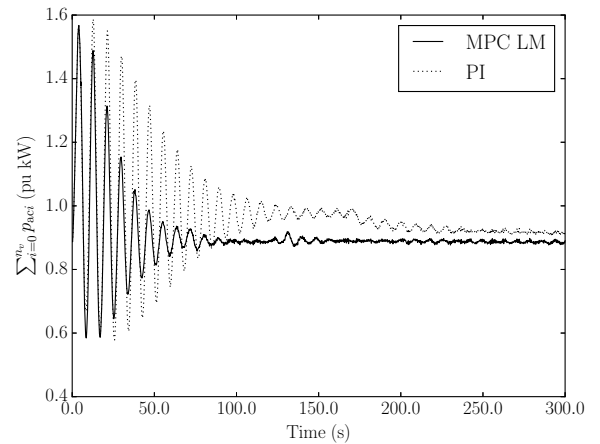


Fig. 19. DC grid power losses with 3 s delay. Stochastic wind case.

The following local PI-based AGC is augmented to return the dc power setpoint to its original value:

$$p_{ac}^{\text{ref}}(t) = \int_{t=0}^{t=\infty} k_{I\omega}(\omega_{\text{COI}}(t) - \omega_s) - k_{Iu}(p_{ac}^{\text{ref}}(t) - p_{ac0}^{\text{ref}}) dt \quad (39)$$

where p_{ac0}^{ref} is the nominal VSC power setpoint, $k_{I\omega}$ and k_{Iu} are the integral gains associated with deviations from the nominal frequency and scheduled DC power, respectively.

An additional cost is added to the MPC cost function to penalise deviations of the setpoints p_{ac}^{ref} from their nominal

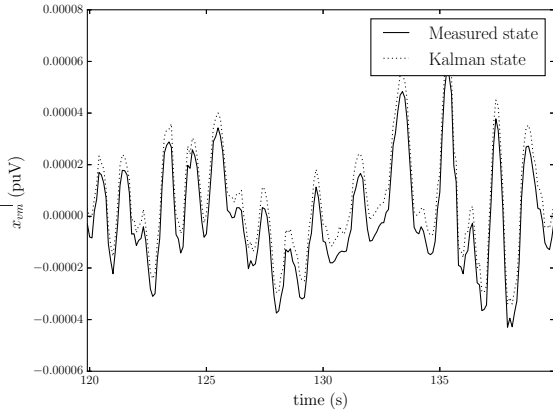


Fig. 20. Kalman filter estimate vs. measurement of VSC voltage regulation state.

values. The new cost function incorporating VSC power setpoint deviation penalties becomes:

$$J(k) = \tilde{\mathbf{x}}_{\omega}^T \mathbf{Q}_{\omega} \tilde{\mathbf{x}}_{\omega} + \tilde{\mathbf{x}}_v^T \tilde{\mathbf{G}} \tilde{\mathbf{x}}_v + \Delta \tilde{\mathbf{u}}^T \mathbf{Q}_u \Delta \tilde{\mathbf{u}} + \tilde{\mathbf{p}}^T \mathbf{Q}_p \tilde{\mathbf{p}}, \quad (40)$$

where $\mathbf{p} = [(p_{ac1}^{\text{ref}}(k) - p_{ac01}^{\text{ref}}) \dots (p_{acn_v}^{\text{ref}}(k) - p_{ac0n_v}^{\text{ref}})]^T$, and weighting matrix $\mathbf{Q}_p = \text{diag}(q_p, \dots, q_p)$.

Simulations are conducted using the wind-free scenario so as to illustrate clearly the effects of penalising the setpoint deviations. Here $\beta_p = 0.5$, $\beta_f = 10$, $K_{P,dc} = 3$, and $K_{I,dc} = 1.7$, which ensure a significant primary and secondary response from the controllers. With regard to the PI controllers $k_{I\omega} = 10$ and $k_{Iu} = 0.05$. For the MPC controller $q_p = 2 \times 10^{-4}$, with the rest of the parameters tuned as in the previous examples. Tuning here was based on trial and error to give desirable system performance while maintaining a stable and damped response. The simulations were carried out for the same scenario as outlined previously, for the loss of a DC line, and comparisons are made with the cases where $k_{Iu} = 0$ for the PI-based control and $q_p = 0$ for the MPC based control.

The resultant frequency and DC power plots can be seen in Figs. 21-25. A number of observations are made with relation to the frequency responses. While the MPC initially results in some larger frequency deviations than the PI within the first 20 s, it quickly stabilises the system to provide a damped frequency response. This larger initial frequency deviation is explained by the MPC seeking to minimise the DC side losses where as can be seen in Fig. 25.

The p_{ac}^{ref} deviation penalty is effective in regulating DC powers in closer proximity to their original scheduled values, as can be seen in Fig. 24. Additionally, for the MPC it provides improved frequency regulation while maintaining the DC power loss minimisation performance. Thus, if it is desired to maintain the DC powers close to their scheduled values, the use of the p_{ac}^{ref} deviation penalty provides several advantages. However, it should be noted that one of the main motivating factors behind the construction of MTDC grids is the ability to exchange of large amounts of reserves over wide areas.

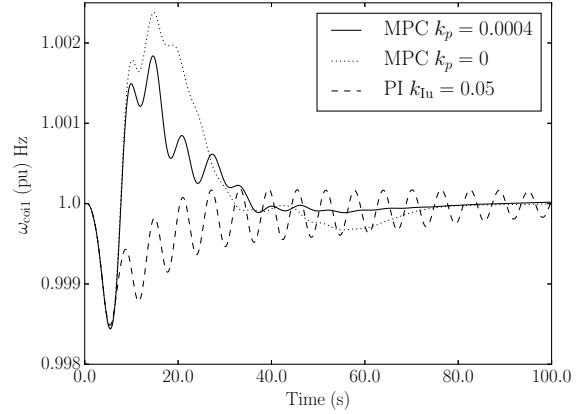


Fig. 21. COI frequency in area 1 for 3 s delay. Penalising VSC setpoint deviations example.

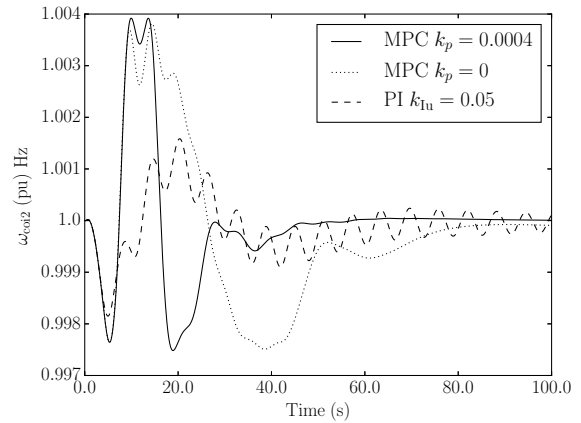


Fig. 22. COI frequency in area 2 for 3 s delay. Penalising VSC setpoint deviations example.

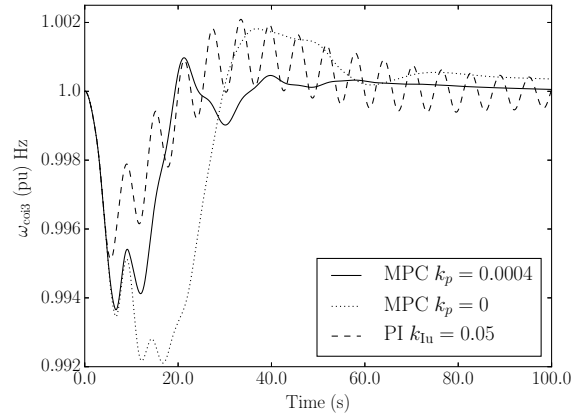


Fig. 23. COI frequency in area 3 for 3 s delay. Penalising VSC setpoint deviations example.

The use of the p_{ac}^{ref} deviation penalties limits the degree to which an AC area will inject power into the DC grid. Thus, the implementation of p_{ac}^{ref} deviation penalties gives practitioners a degree of freedom with system design in terms of determining to what degree DC powers can deviate from their original

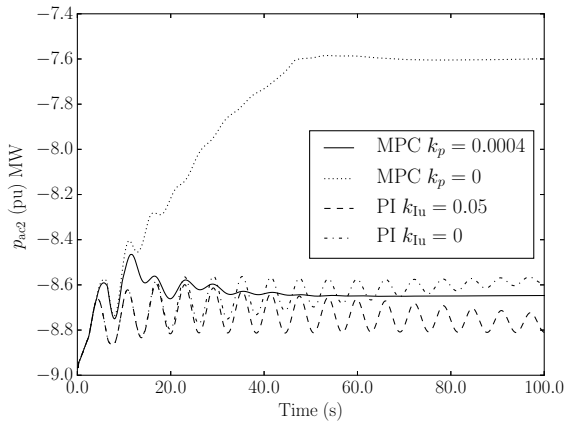


Fig. 24. AC power injected from VSC 2. Penalising VSC setpoint deviations example.

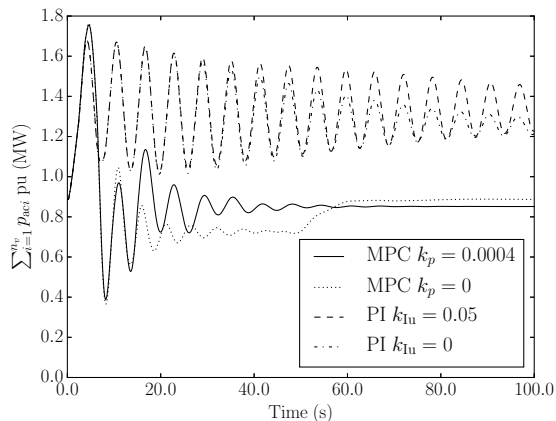


Fig. 25. Losses in DC grid. Penalising VSC setpoint deviations example.

scheduled setpoints.

VI. CONCLUSIONS AND FUTURE WORK

In this paper, a model predictive control (MPC) algorithm was proposed for coordinating automatic generation control (AGC) in ac systems connected to multi-terminal high voltage dc (MTDC) grids. The MPC is designed to regulate frequency errors and minimise dc power grid losses. The use of ‘soft’ constraints based on slack variables is also investigated as a means of maintaining dc voltages within upper and lower bounds. A Kalman filter is designed to provide state estimates for the MPC from a subset of measurements. Finally, the effect of limiting DC power setpoint deviations from their nominal values was investigated. Custom software was developed in the ‘Dome’ simulation environment to allow this control to be applied to arbitrary ac/dc grid configurations. It was found that the MPC controllers provided significant improvements over PI controllers in terms of frequency regulation and damping, and dc grid power loss minimisation.

Future work will look at applying this technique for the regulation of realistic models of large scale ac/dc grids, such as the European Supergrid. Additionally, distributed MPC will

be evaluated as a means of applying this control in a non-centralised fashion to coordinate the actions of Transmission Systems Operators. While an unconstrained Kalman filter is used in this paper, it would be of interest to investigate the use of moving horizon estimation techniques to frame the estimation problem as an optimisation problem that could consider constraints on the estimated state.

ACKNOWLEDGMENT

This material is based upon works supported by the Science Foundation Ireland, by funding Paul Mc Namara under Grant No. SFI/09/SRC/E1780 and Federico Milano under Investigator Programme Grant No. SFI/15/IA/3074. The opinions, findings and conclusions or recommendations expressed in this material are those of the author and do not necessarily reflect the views of the Science Foundation Ireland. Federico Milano and Paul Mc Namara additionally benefit from the financial support of EC Marie Skłodowska-Curie Career Integration Grant No. PCIG14-GA-2013-630811.

REFERENCES

- [1] D. Van Hertem and M. Ghandhari, “Multi-terminal VSC HVDC for the European supergrid: Obstacles,” *Renewable and sustainable energy reviews*, vol. 14, no. 9, pp. 3156–3163, 2010.
- [2] N. Chaudhuri, B. Chaudhuri, R. Majumder, and A. Yazdani, *Multi-terminal direct-current grids: modeling, analysis, and control*. John Wiley & Sons, 2014.
- [3] G. Tang, Z. He, H. Pang, X. Huang, and X.-P. Zhang, “Basic topology and key devices of the five-terminal DC grid,” *CSEE Journal of Power and Energy Systems*, vol. 1, no. 2, pp. 22–35, 2015.
- [4] J. Dai, “Frequency control coordination among non-synchronous AC areas connected by a multi-terminal HVDC grid,” Ph.D. dissertation, Supélec, France, 2011.
- [5] I. Sanz, B. Chaudhuri, and G. Strbac, “Inertial response from offshore wind farms connected through DC grids,” *IEEE Transactions on Power Systems*, vol. 30, no. 3, pp. 1518–1527, 2015.
- [6] T. Haileselassie, A. Endegnanew, and K. Uhlen, “Secondary control in multi-terminal VSC-HVDC transmission system,” in *Proceedings of the IEEE Power & Energy Society General Meeting*. Denver, CO, USA: IEEE, 2015, pp. 1–5.
- [7] M. Andreasson, R. Wiget, D. Dimarogonas, K. Johansson, and G. Andersson, “Distributed secondary frequency control through multi-terminal HVDC transmission systems,” in *Proceedings of the IEEE Conference on Decision and Control*, Osaka, Japan, 2015.
- [8] J. Maciejowski, *Predictive Control with Constraints*. Harlow, England: Prentice Hall, 2002.
- [9] A. Ersdal, L. Imsland, and K. Uhlen, “Model predictive load-frequency control,” *IEEE Transactions on Power Systems*, vol. 31, no. 1, pp. 777–785, 2015.
- [10] M. Shiroei, M. Toulabi, and A. Ranjbar, “Robust multivariable predictive based load frequency control considering generation rate constraint,” *International Journal of Electrical Power & Energy Systems*, vol. 46, pp. 405–413, 2013.
- [11] P. Mc Namara, R. Meere, T. O’Donnell, and S. McLoone, “Control strategies for automatic generation control over MTDC grids,” *Control Engineering Practice*, vol. 54, pp. 129–139, 2016.
- [12] M. Almalkhi and I. Hiskens, “Model-predictive cascade mitigation in electric power systems with storage and renewables—part I: theory and implementation,” *IEEE Transactions on Power Systems*, vol. 30, no. 1, pp. 67–77, 2015.
- [13] M. Moradzadeh, R. Boel, and L. Vandevelde, “Voltage coordination in multi-area power systems via distributed model predictive control,” *IEEE Transactions on Power Systems*, vol. 28, no. 1, pp. 513–521, 2013.
- [14] A. Fuchs, M. Imhof, T. Demiray, and M. Morari, “Stabilization of large power systems using VSC-HVDC and model predictive control,” *IEEE Transactions on Power Delivery*, vol. 29, no. 1, pp. 480–488, 2014.
- [15] I. M. Sanz, B. Chaudhuri, and G. Strbac, “Coordinated corrective control for transient stability enhancement in future Great Britain transmission system,” in *Proceedings of the Power Systems Computation Conference (PSCC)*, June 2016, pp. 1–7.

- [16] M. Carrizosa, F. Navas, G. Damm, and F. Lamnabhi-Lagarigue, "Optimal power flow in multi-terminal HVDC grids with offshore wind farms and storage devices," *International Journal of Electrical Power & Energy Systems*, vol. 65, pp. 291–298, 2015.
- [17] P. Mc Namara, R. R. Negenborn, B. de Schutter, G. Lightbody, and S. McLoone, "Distributed MPC for frequency regulation in multi-terminal HVDC grids," *Control Engineering Practice*, vol. 46, pp. 176–187, 2016.
- [18] A. Fuchs, S. Mariétoz, M. Larsson, and M. Morari, "Grid stabilization through VSC-HVDC using wide area measurements," in *Proceedings of PowerTech*, June 2011, pp. 1–6.
- [19] P. Mc Namara, Á. Ortega, and F. Milano, "Model predictive control based AGC for multi terminal DC grids," in *Proceedings of the IEEE PES General Meeting*, Boston, MA, 2016.
- [20] P. Mc Namara and F. Milano, "MPC based AGC for AC/DC grids with delays and voltage constraints," in *submitted to the IEEE PES General Meeting*, Chicago, IL, USA, 2017.
- [21] F. Milano, "A python-based software tool for power system analysis," in *Proceedings of the IEEE PES General Meeting*, Vancouver, BC, Canada, July 2013, pp. 1–5.
- [22] —, "Semi-Implicit Formulation of Differential-Algebraic Equations for Transient Stability Analysis," *IEEE Transactions on Power Systems*, vol. 31, no. 6, pp. 4534–4543, Nov 2016, in press.
- [23] —, *Power system modelling and scripting*. Springer Science & Business Media, 2010.
- [24] P. Kundur, *Power System Stability and Control*. Mc-Graw Hill, New York, 1994.
- [25] J. Rawlings and D. Mayne, *Model Predictive Control: Theory and Design*. Madison, Wisconsin: Nob Hill Publishing, 2009.
- [26] R. R. Labbe Jr., *Kalman and Bayesian filters in Python*, available online: robotics.itee.uq.edu.au/elec3004/2015/tutes/Kalman_and_Bayesian_Filters_in_Python.pdf, 2016.



Paul Mc Namara (S11,M13) received his Ph.D. degree in centralized and distributed control of the smart grid from University College Cork, Cork, Ireland in 2012. He is currently a Senior Researcher with the Electricity Research Centre, University College Dublin, Dublin, Ireland. His current research interests include the application of centralized and distributed control and optimization techniques to electrical power systems.



Federico Milano (S'02, M'04, SM'09, F'16) received from the Univ. of Genoa, Italy, the ME and Ph.D. in Electrical Eng. in 1999 and 2003, respectively. From 2001 to 2002 he was with the Univ. of Waterloo, Canada, as a Visiting Scholar. From 2003 to 2013, he was with the Univ. of Castilla-La Mancha, Spain. In 2013, he joined the Univ. College Dublin, Ireland, where he is currently Professor of Power Systems Control and Protections. His research interests include power system modeling, stability analysis and control.